

# Laser-based imaging of individual carbon nanostructures

Robin W. Havener<sup>1</sup>, Adam W. Tsen<sup>1</sup>, Hee Cheul Choi<sup>2\*</sup> and Jiwoong Park<sup>3,4\*</sup>

Cornell University, USA and Pohang University of Science and Technology, Korea

Laser-based imaging and characterization of individual nanostructures provides significant advantages over other imaging techniques, such as scanning probe microscopy and electron microscopy, by allowing simultaneous imaging and spectroscopic measurements. Laser-based techniques also involve simpler sample preparation, cause minimal sample damage and provide high-throughput measurements over large sample areas. In this article, we review recent progress in this field focusing on applications in the study of individual carbon nanostructures, mainly carbon nanotubes and graphene. Absorption, Rayleigh, Raman and photoluminescence techniques will be discussed for optical-based detection, and photocurrent and photothermal current techniques will be discussed for electrical detection. Each optical technique relies on a different physical process, allowing spectroscopic investigation of the fundamental optical, thermal and optoelectronic processes for individual nanoscale carbon structures. In addition, we will compare the various advantages of wide-field and focused (confocal) laser excitation/detection geometries and discuss ongoing efforts to overcome the speed and resolution limitations of laser-based imaging.

Carbon nanotubes (CNTs) and graphene, one- and two-dimensional  $sp^2$  carbon nanostructures, have played a central role in nanoscale science and technology in the past two decades, showing many remarkable electrical, mechanical and chemical properties not found in other materials [1,2]. The rapid expansion of this field has been largely fueled by the use of well-established microscopy techniques to image and characterize these materials. For instance, transmission electron microscopy (TEM) was used to confirm the tubular structure of CNTs in the seminal papers by Iijima in 1991 [3] and 1993 [4], while the optical imaging technique first used by Geim and Novoselov [5] enabled rapid identification of single-layer exfoliated graphene. Atomic force microscopy (AFM) and scanning electron microscopy (SEM) are also widely used to locate individual nanostructures for later incorporation into various electronic and optical device geometries.

As the electronic and optical properties of CNTs are strongly dependent on their length, diameter, number of walls, bundling and chiral index ( $n,m$ ), it is important to differentiate between different types of CNTs in a heterogeneous, as-grown sample. Diffraction-mode TEM [6] and scanning tunneling microscopy (STM) have enabled identification of the chiral indices of single-walled nanotubes (SWNTs) [7]. Unlike CNTs, the crystal structure of an exfoliated single-layer graphene sample is well-known, but with the recent development of chemical vapor deposition (CVD) graphene growth [8–10], there is renewed interest in applying various imaging techniques to characterize the number of layers, as well as the structure and quality of graphene resulting from various growth parameters. For example, low-energy electron diffraction [11] and SEM [12] techniques have been used to study the growth dynamics of CVD graphene, and TEM has been used to map CVD graphene grains [13,14].

However, traditional non-optical techniques have several disadvantages. Scanning probe techniques such as STM and AFM are generally slow, limiting their ability to characterize many nanotubes or graphene

over a large area. Techniques such as SEM and AFM provide limited information about nanotube chirality or graphene atomic structure, whereas more informative techniques such as TEM and STM involve more complicated sample preparation procedures, precluding many device geometries. Optical microscopy has many advantages over these techniques. Not only can images be acquired rapidly, allowing large-scale imaging with high throughput, but optical techniques also require minimum sample preparation, cause little damage to the sample and can provide spectroscopic information probing electronic and vibrational processes.

Impressive progress has been made recently in applying various laser-based imaging techniques, including absorption, Rayleigh, Raman and photoluminescence (PL) microscopy, to image and characterize individual SWNTs in various geometries. Using these techniques, it has become possible to measure the chiral indices of hundreds to thousands of SWNTs in just minutes over a millimeter-scale sample area [15], and also to monitor the growth of SWNTs in real time [16]. Laser-based imaging techniques, and Raman in particular, have also proved to be important characterization tools for graphene [17]. Moreover, laser-based excitation can be used to generate spatial maps of non-optical properties, such as electrical and thermal responses, of CNTs and graphene, thus providing additional means of optoelectronic imaging.

In this article, we review the recent developments in laser-based imaging of carbon nanostructures. We briefly discuss the electronic structure of SWNTs and graphene, which provides the fundamental basis for all optical and optoelectronic processes in these materials, and then describe imaging techniques for SWNTs involving optical Rayleigh, absorption, Raman and PL detection. The performance of these techniques on the two main instrumentation platforms, either confocal or wide-field illumination/detection geometry, is also compared. The uses of such techniques for graphene imaging are discussed, and in closing

\*Corresponding authors. Email: jpark@cornell.edu, choihc@postech.ac.kr

<sup>1</sup>School of Applied and Engineering Physics, Cornell University, Ithaca, NY 14853, USA

<sup>2</sup>Department of Chemistry and Division of Advanced Materials Science, Pohang University of Science and Technology (POSTECH), San 31, Hyoja-Dong, Nam-Gu, Pohang 790-784, Korea

<sup>3</sup>Department of Chemistry and Chemical Biology, Cornell University, Ithaca, NY 14853, USA

<sup>4</sup>Kavli Institute at Cornell for Nanoscale Science, Cornell University, Ithaca, NY 14853, USA

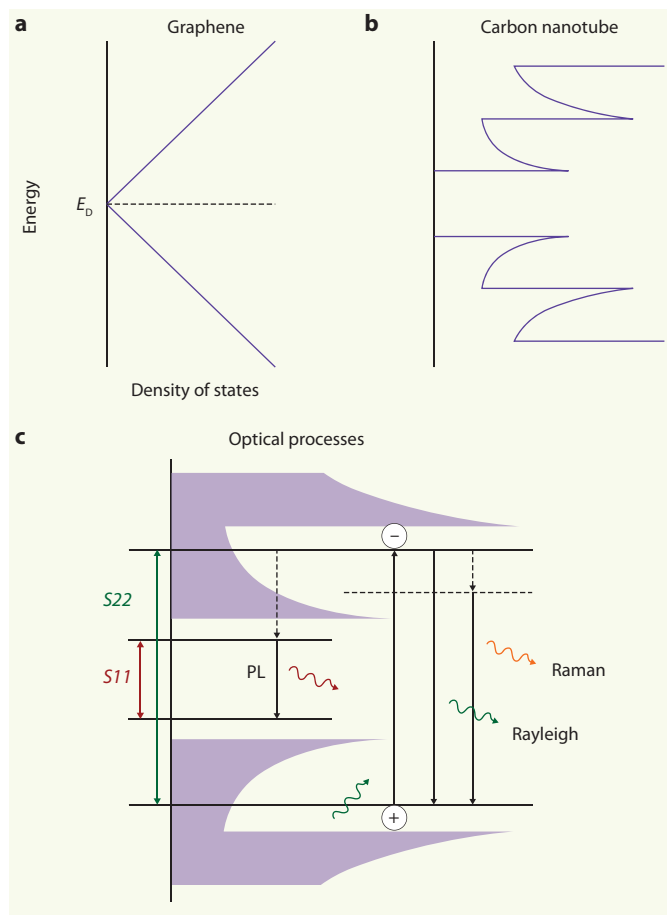


**Figure 1.** (a) Schematic illustration of the density of electronic states (DOS) with respect to energy for graphene. The DOS increases linearly with energy. (b) Unlike graphene, the DOS of SWNTs exhibits sharp peaks (van Hove singularities). This particular SWNT is semiconducting because the DOS goes to zero over a finite energy range, forming an electronic bandgap. (c) Allowed optical processes in SWNTs. Light with energy corresponding to an allowed optical transition (S11, S22, etc.) can create an exciton (bound electron-hole pair). Excitonic energy levels are hundreds of meV lower than the vHs peaks in the continuum electronic states. Resonance of the illumination energy with an allowed excitonic transition enhances elastic (Rayleigh) scattering, and also enhances Raman scattering, where the emitted photon is red (Stokes, shown) or blue (anti-Stokes) shifted due to the creation or destruction of a phonon. Optically excited excitons can also decay through non-radiative processes to the lowest allowed energy state, and subsequently emit photoluminescence.

we review recent results obtained using electrical detection methods and the prospects for future developments and applications.

### Electronic structure of carbon nanotubes and graphene

There exist many comprehensive review articles on the closely related electronic structures of CNTs and graphene [1,18]. As a brief overview, the optical properties of graphene originate from its unique band structure, which has cone-like conduction and valence bands near the charge neutrality energy (or Dirac point,  $E_D$ ). Graphene has a linearly increasing density of states away from  $E_D$  (Figure 1(a)) and a linear dispersion relation ( $E = v_F \hbar |k|$ , where  $v_F$  is the Fermi velocity and  $k$  is the wavevector). This results in a uniform (~2.3%) optical absorption over most of the visible and near-infrared spectrum [19]. In contrast, SWNTs show optical resonance peaks, reflecting similar resonances in their electronic structure. Due to the periodic boundary condition on the tube circumference, the electronic states of SWNTs consist of multiple subbands that are roughly equivalent to the cutting-lines through the surface of the graphene band structure.

In a non-interacting, single-particle picture, these one-dimensional subbands give rise to resonance peaks (van Hove singularities; vHs) in the SWNT density of states (Figure 1(b)). For some SWNT chiralities, there is a finite density of states between the lowest vHs peaks, making them metallic (M), whereas the remaining chiralities are semiconducting (S). Electron-electron interactions modify this simple picture both for the ground and excited states. In particular, it has been shown that while the electrical conductance of SWNTs is best described by the properties of the continuum states, optical resonances in SWNTs are mainly due to excitonic states, even for metallic nanotubes [20,21]. Depending on the associated subbands, such resonances are denoted by S11, S22, M11 and so on.

Figure 1(c) illustrates the various allowed optical processes in SWNTs: absorption, Rayleigh scattering, Raman scattering and PL. It is clear that the efficiency of all of these processes is strongly influenced by the underlying electronic structure. Sharp optical peaks are observed when the energy of the illuminating or emitted photons is equal to the energy of an allowed excitonic state.

Much theoretical and experimental work has been conducted to understand the correlation between SWNT chiral indices ( $n,m$ ) and the resonances associated with the excitonic states and vHs. Raman, PL, Rayleigh and absorption spectroscopies have all been used to probe both ensembles and individual SWNTs, providing direct measurements of interband transition energies. By identifying the resonance energies and comparing the results with theory or direct chiral measurements (such as TEM diffraction [22]), it is possible to determine whether an individual SWNT is metallic or semiconducting, as well as identify its chiral index. However, care must be taken to take the local environment into account, which can cause systematic peak shifts and broadening [23]. In general, two resonance energies need to be measured to assign the two chiral indices that characterize an individual SWNT, unless other information (such as the nanotube diameter) is known [24–26].

### Modes of illumination and detection

All laser-based imaging techniques are performed using commercial or customized optical microscopes equipped with three essential components: an excitation laser and delivery optics (illumination), an optical detector and collection optics (detection), and a moveable stage (sample positioning/image formation). Figure 2 shows schematic diagrams of the typical configurations of these components for different modes of illumination and detection. Although each technique often requires a dedicated setup with specialized components for optimal performance, there are several features common to all configurations.

Samples are optically excited using one of two illumination schemes, as shown in Figure 2(a). For confocal imaging, a focused laser beam with wavelength  $\lambda_{ex}$  (spot size typically smaller than 1  $\mu\text{m}$ ) is used to illuminate the sample surface. The laser spot is raster-scanned across the sample, and optical signals can be collected as a function of spot position to construct an image. Either a motorized stage (~100 nm resolution with a large scan range) or a piezoelectric stage (better than 10 nm resolution with a limited range of ~100  $\mu\text{m}$ ) can be used for this purpose. For wide-field imaging, a larger area of the sample is illuminated and the light emitted by the sample is collected using an array detector, such as a charge-coupled device (CCD). Both of these techniques have various advantages and disadvantages, which will be discussed in more detail later.

Optical detection methods fall into two categories depending on the optical process being probed (Figure 2(b)). For measurements of Rayleigh scattering and absorption, the wavelength of the detected light (scattered or transmitted) is the same as the excitation wavelength ( $\lambda_{ex}$ ). As all materials exhibit scattering and absorption, the background signal from the sample substrate is an issue. Additional means of enhancing the signal-to-noise ratio are therefore necessary, such as dark-field illumination for Rayleigh scattering, Raman and PL, on the

other hand, are inelastic processes, where the emission wavelength  $\lambda_{em}$  is different from  $\lambda_{ex}$ . As a result, background scattering can be easily filtered out using either a bandpass filter or a spectrometer, yielding a high signal-to-noise ratio.

To fully characterize a SWNT sample, wavelength-resolved imaging is required. Rayleigh scattering and absorption as a function of wavelength show resonance peaks corresponding to excitonic transitions, as discussed in the previous section. In order to scan  $\lambda_{ex}$ , a tunable laser (e.g. Ti-sapphire) or a broadband light source (e.g. supercontinuum laser) with a monochromator is required. In Raman and PL, the emission spectra measured at a fixed  $\lambda_{ex}$  provide additional information, such as the phonon spectrum (Raman) and the lowest S11 resonance of semiconducting SWNTs (PL). In order to resolve  $\lambda_{em}$  at a fixed  $\lambda_{ex}$ , a spectrometer or bandpass filter is needed on the detection end of the optics. As Raman and PL signals are low when  $\lambda_{ex}$  is off-resonance, a two-dimensional spectral mapping ( $\lambda_{ex}$  and  $\lambda_{em}$ ) of these inelastic processes is necessary in order to obtain a full characterization of a heterogeneous SWNT sample.

The ease of detecting these optical processes is also determined by their respective efficiencies, which are typically defined in the literature in units of scattering or absorption cross-section ( $\text{cm}^2/\text{C atom}$ ,  $\text{cm}^2/\text{unit CNT length}$ , or  $\text{cm}^2/\text{sr}$  for an entire CNT), or luminescence quantum yield (ratio of emitted to absorbed photons). The absorption cross-section on resonance for single SWNTs has been measured to be of the order of  $1 \times 10^{-17} \text{ cm}^2/\text{C atom}$  [27–29], or roughly 30% of the physical cross-section of the nanotube [29]. The Rayleigh scattering cross-section on resonance is roughly two to three orders of magnitude smaller [29], and is proportional to the nanotube diameter, as predicted by the classical theory of radiation from a thin cylinder. Raman scattering is at least several orders of magnitude less efficient than either of these processes, although only a few experimental approximations of Raman scattering cross-section exist in the literature. Recently, the radial breathing mode (RBM) cross-section was estimated to be of the order of  $10^{-22} \text{ cm}^2/\text{sr}$  for single nanotubes on silicon [30], corresponding to  $\sim 10^{-27} \text{ cm}^2/\text{C atom}$  (assuming that the nanotubes were 1 nm in diameter and 100 nm in length). Photoluminescence quantum yields have been measured to be as high as  $\sim 7\%$  for suspended nanotubes [31] and  $\sim 20\%$  in solution [32]. However, the local environment has a particularly strong effect on the yield of this process, such that PL can be quenched in nanotube bundles [33] or in nanotubes in contact with substrates [31] to the point where it is undetectable. The Raman scattering cross-section of nanotubes on substrates can also be reduced by as much as one or two orders of magnitude with respect to that for suspended nanotubes [34–36].

Finally, when imaging SWNTs, it is important to consider the polarization of the incident and detected light with respect to the nanotube axis. In general, the intensity of the detected signal varies according to  $\cos^2$  of the angle between the incident linear polarization and the nanotube axis due to the antenna effect [24,37,38], so light polarized along the nanotube axis is usually desirable for imaging applications. However, different polarizations can be used to probe processes in different symmetries. For example, light polarized perpendicular to the nanotube axis selectively excites  $S(M)_{i\pm 1}$  excitonic transitions [1], and different Raman phonon symmetries are active depending on the relative orientations of the incident and scattered light with respect to the nanotube axis [39].

### Rayleigh imaging of carbon nanotubes

The intensity of Rayleigh scattering in SWNTs is strongest at wavelengths corresponding to optical excitonic transitions [24,40] (Figure 2(a)), allowing the chirality of individual nanotubes to be determined. The efficiency of Rayleigh scattering (or absorption) is quantified using the cross-section width ( $\delta_{scatt}$  or  $\delta_{abs}$ ), defined as the scattering (or absorption) cross-section per unit length. This parameter is a function of the wavelength-dependent dynamic optical

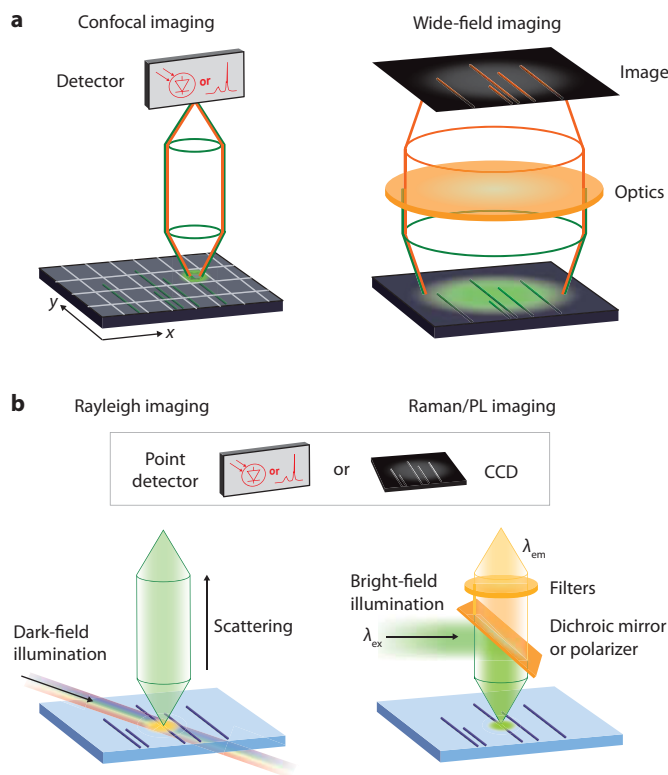


**Figure 2.** (a) Confocal and wide-field illumination schemes. Confocal illumination is provided by a focused spot, and detection is performed using a photodiode or spectrometer. An image can be reconstructed pixel-by-pixel after scanning the confocal spot over the sample. Wide-field illumination is provided by a much larger spot, and the image (after various optics and/or filters) is projected directly onto an array detector. (b) Optical detection methods for Rayleigh and Raman/PL imaging. Rayleigh illumination is performed in a dark-field geometry to eliminate specular reflections. Illumination can be provided by a broadband or tunable wavelength source. Raman/PL is typically performed in a bright-field geometry, and the incident wavelength is eliminated through a series of filters or monochromators. Both detection methods are compatible with both confocal and wide-field illumination schemes, as illustrated in (a).

conductivity,  $\sigma(\lambda_{ex})$  [29], a quantum mechanical quantity determined by the electronic structure of SWNTs. In general,  $\delta_{abs}$  is proportional to  $\text{Re}[\sigma(\lambda_{ex})]$  and  $\delta_{scatt}$  is proportional to  $|\sigma(\lambda_{ex})|^2$ . Essentially all SWNTs have at least one transition in the visible range (1.5–2.5 eV), which typically corresponds to the M22, S33 or S44 transitions for nanotubes with diameters between 1.5 and 2.5 nm [41]. All nanotubes on a sample can therefore be probed using a laser source with a sufficiently tunable or broadband wavelength range, such as a supercontinuum laser.

In Rayleigh imaging, the elastically scattered light is collected in a dark-field geometry, eliminating the incident beam from the detection pathway (Figure 2(b)). Even so, the Rayleigh scattering signal from a SWNT on a substrate is much weaker than the scattering from the substrate itself, requiring additional sample preparation in order to make Rayleigh imaging a viable technique. The first Rayleigh scattering spectrum for a SWNT was obtained in a confocal geometry on fully suspended nanotubes grown across trenches (Figure 3(a)) [24]. This geometry provides spectra with a high signal-to-noise ratio for pristine nanotubes, and enables other optical measurements (Raman [24], absorption [21]) and TEM characterization [22]. However, spatial information is limited in this geometry, and the fragility of the samples makes further device fabrication difficult.

Recently, Rayleigh imaging and spectroscopy in a wide-field geometry has been accomplished by ‘optically suspending’ SWNTs on a transparent substrate (Figures 3(b) and (c)) [15,29]. Here, most of the elastic

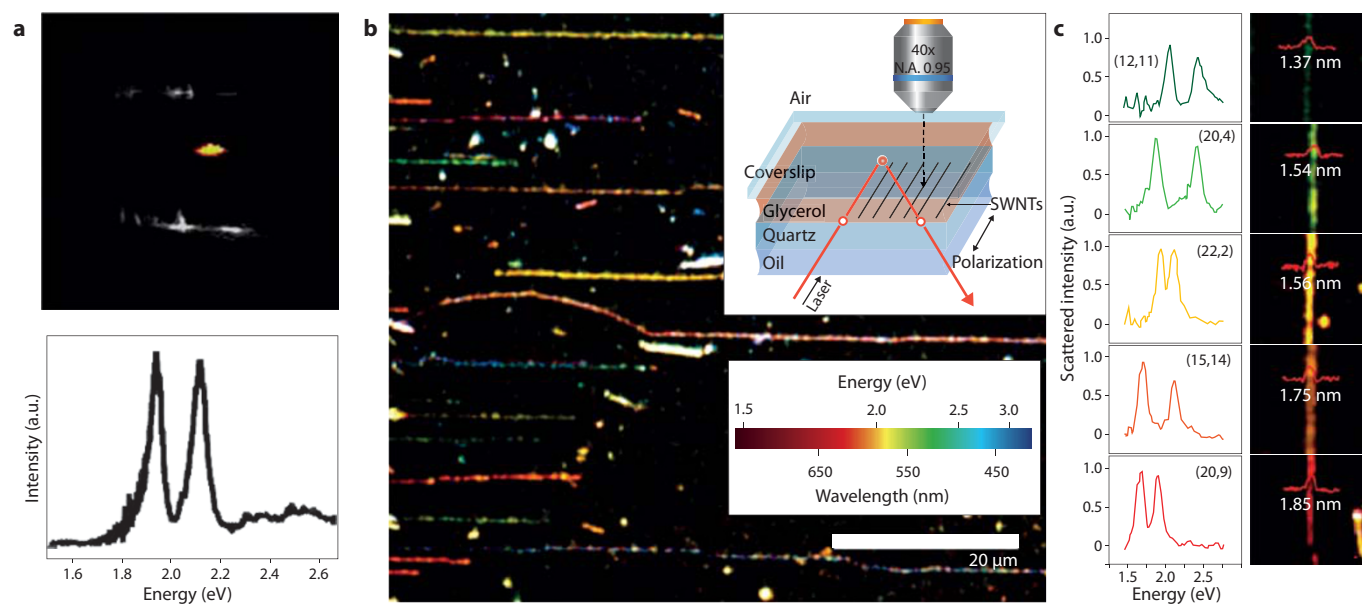


**Figure 3.** (a) Confocal Rayleigh imaging and spectroscopy of a suspended nanotube. (Top) The nanotube is illuminated at a focused spot by a white broadband source (supercontinuum laser), but the scattered light is colored (yellow) due to enhancement of scattering at certain wavelengths. (Bottom) The spectrum of Rayleigh-scattered light from a single SWNT, which exhibits sharp peaks. Adapted from Ref. 24 (© 2004 AAAS). (b) A color image of many nanotubes on a quartz substrate, where the colors correspond to the energies at which Rayleigh scattering is the strongest. The nanotubes were illuminated in a wide-field geometry, but scattering from the substrate was suppressed by covering the sample with an index-matching medium (see inset). (c) Individual spectra and chirality assignments for nanotubes obtained by wide-field Rayleigh imaging, showing similar features to (a). Adapted from Ref. 15 (© 2011 ACS).

scattering from the sample substrate is suppressed by coating it with an index-matching medium (Figure 3(b)). Instead of collecting a Rayleigh spectrum at a fixed confocal point, a series of wide-field CCD images is taken while varying  $\lambda_{\text{ex}}$ . Analysis then gives the Rayleigh spectra for every pixel of the large field of view. A color-projected image of such an array of SWNTs is shown in Figure 3(b), where the color corresponds to the Rayleigh resonance energy. The Rayleigh images and spectra of a series of semiconducting SWNTs are shown in Figure 3(c), showing that chirality assignments can be made for many nanotubes simultaneously.

The wide-field geometry also enables measurements that are difficult or impossible in the confocal geometry. For example, the high-throughput spatial information obtained using this technique can be used to map the location of all nanotubes over a large ( $80 \times 80 \mu\text{m}^2$ ) area in minutes, and interesting features, such as location at which the chirality of a nanotube changes, can be identified easily and rapidly. Furthermore, wide-field measurements have provided evidence of long-range inter-nanotube coupling through either Rayleigh peak shifts [15] or the transfer of brightness between nanotubes [29] as far as 300 nm apart. As the incident power per unit area and the detection efficiency are well-defined in the wide-field geometry, the absolute value of  $\delta_{\text{scatt}}$  can be measured directly (typically 0.2–2.3 pm on resonance) [29], which also suggests that  $\delta_{\text{abs}}$  on resonance is equivalent to approximately 30% of the nanotube diameter.

### Absorption imaging of carbon nanotubes

As discussed above, absorption spectra exhibit many of the same features as Rayleigh scattering spectra because both processes are a function of  $\sigma(\lambda_{\text{ex}})$ . Although on-resonance  $\delta_{\text{abs}}$  for nanotubes is roughly three orders of magnitude larger than on-resonance  $\delta_{\text{scatt}}$  [29], the absorption spectra for individual nanotubes are difficult to detect because the absorbed power is still many orders of magnitude less than the transmitted power, even for a tightly focused laser spot. The absorption spectra for individual suspended nanotubes have been measured in a confocal geometry using a lock-in technique [21], but there is no report to date of spatially resolved imaging based on direct absorption measurements of SWNTs.

Only indirect measurements have been used to produce absorption-related images. In one technique, known as photothermal heterodyne imaging [42], a confocal laser beam is used to excite an individual SWNT, with the local absorption resulting in heating of the SWNT and the surrounding medium. This causes a change in the index of refraction of the medium, which is then detected using a separate colorized laser. Confocal images of CNTs can be obtained with intensity proportional to their degree of absorption at a specific wavelength (Figure 4(a), inset) [43], or an absorption spectrum at a fixed location can be taken by scanning the wavelength of the excitation (heating) laser (Figure 4(a)) [28,43].

### Raman imaging of carbon nanotubes

Carbon nanotubes exhibit several strong Raman peaks [40], and the Raman spectrum at a fixed  $\lambda_{\text{ex}}$  provides detailed information about the CNT type and quality. As shown in Figure 5(a), the RBM has a frequency given by a simple function of the nanotube diameter; the G-band peaks have lineshapes and positions dependent on the nanotube type (S/M) [44], chirality [45] and carrier doping [46]; and the D/G band intensity ratio indicates the presence of defects. The approximate wavenumbers and peak widths of these Raman-active modes are known, so the background signal can be filtered out, allowing images with a high signal-to-noise ratio to be obtained despite the inefficiency of the Raman process (several orders of magnitude weaker than Rayleigh scattering). The Raman intensity increases dramatically when the incident or scattered light corresponds to an excitonic resonance energy (resonant Raman, see Figure 1(b)), which is in the regime in which most measurements are performed.

Raman imaging is usually performed in a confocal geometry (micro-Raman imaging), with the immediate advantage that a full Raman spectrum can be obtained at each diffraction-limited pixel. An image can then be obtained by mapping the spatial variation of a particular spectral feature (peak intensity [47], position or width). A series of micro-Raman images acquired over different excitation wavelengths can also be used to identify the chirality of an individual nanotube [48]; the position of the RBM mode provides the diameter

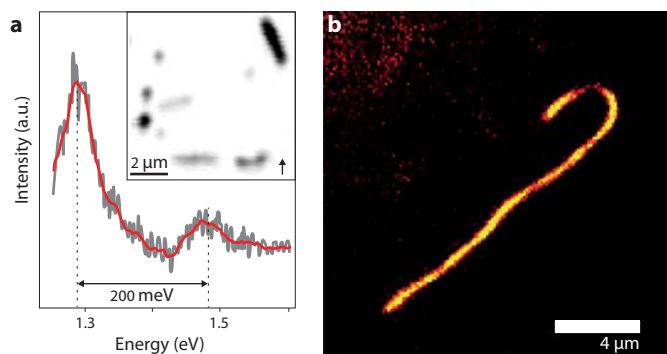


**Figure 4.** (a) Absorption spectrum obtained for a single nanotube by photothermal heterodyne imaging (PHI). A sideband is observed at  $\sim 200$  meV above the expected E11 transition, corresponding to a (G-band) Raman process. (Inset) A PHI image of CNTs on a glass coverslip at 565 nm (arrow indicates incident polarization). Adapted from Ref. 43 (© 2007 ACS). (b) A PL image of a long (6,5) SWNT in solution, illuminated at 561 nm. Adapted from Crochet *et al.*, 219th ECS Meeting, Abstract #1728, 2011 (© 2011 The Electrochemical Society).

of a specific nanotube, while measurements of RBM intensity vs.  $\lambda_{\text{ex}}$  provide resonance energies.

However, micro-Raman imaging is inherently slow due to the small Raman cross-section width and the need to limit the laser intensity below the damage threshold ( $\sim 40$  mW  $\mu\text{m}^{-2}$  for CNTs on a substrate [1]). Acquiring a full spectrum at each point typically takes seconds, such that a large diffraction-limited image could take hours to obtain. By eliminating the spectrometer and using bandpass filters instead, a confocal G-band image can be acquired in a shorter time (as short as 15 ms per pixel [49], see Figure 5(a)), reducing the imaging time to  $\sim 10$  min for a  $100 \times 100 \mu\text{m}^2$  image (500 nm pixel size).

For even faster Raman imaging, an alternative is to use a wide-field illumination geometry. By increasing the illumination spot size, the laser power can be increased by orders of magnitude over that typically used for confocal Raman imaging while keeping the intensity low [50]. Large, diffraction-limited images can be acquired in seconds (Figure 5(b)), allowing for rapid sample mapping and the study of real-time processes such as nanotube growth [16]. Filters can be used to select for imaging of a specific Raman band [34,50], and high-resolution Raman spectra can be obtained along a line in such an image (selected by a slit at the image plane) using an imaging spectrometer.

Although not all of the nanotubes on the sample substrate will be resonant with a single laser during Raman imaging, it has been found that the G-band Raman signals of approximately two thirds of the nanotubes are strong enough for imaging using a single laser line [49,50]. This suggests that only two or three excitation wavelengths may be required to image all of the SWNTs present in the imaging field.

### Photoluminescence imaging of carbon nanotubes

Photoluminescence spectroscopy is a powerful tool for measuring the resonance energies of nanotubes in solution [25,51], thus providing an essential characterization method for growth and post-processing techniques such as purification and functionalization. In addition, the strong PL signal from carbon nanotubes and its response to the surrounding environment can be used as an infrared probe for biosensing applications [32,52]. With proper sample preparation, SWNTs in solution exhibit a PL signal that is bright enough to allow video-rate PL imaging (Figure 4(b)).

In many ways, PL spectroscopy is well-suited for imaging individual nanotubes; like Raman spectroscopy, any background elastic scattering can be filtered out and the magnitude of the PL signal can be much larger than that of the Raman signal (as much as 7% of  $\delta_{\text{abs}}$

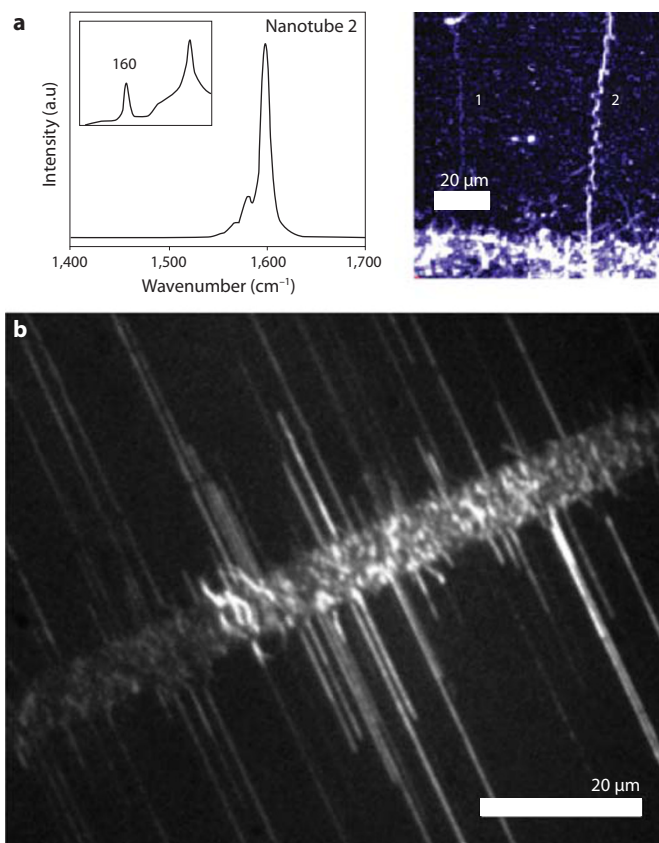


**Figure 5.** (a) A typical SWNT Raman spectrum. The G-band lineshape exhibits two peaks, and the RBM position (inset) indicates the nanotube diameter. These data were acquired for nanotube 2 (right), shown in a spatially resolved confocal G-band image. The SWNTs are grown from a catalyst pad (white area at the bottom of the image). Adapted from Ref. 49 (© 2007 ACS). (b) A wide-field G-band Raman image of aligned CNTs grown on a quartz substrate from a lithographically defined catalyst pad, similar to (a). The image was acquired using a 3 W, 532 nm laser with a  $\sim 80 \mu\text{m}$  illumination spot size and a 20 s acquisition time (courtesy of S. Y. Ju, unpublished data).

for suspended nanotubes [31]). Indeed, PL spectroscopy has been performed in both confocal [26,37] and wide-field [31,53] geometries. However, there are several disadvantages that prevent the widespread adoption of this technique for nanotube imaging, especially for SWNTs on a substrate. Metallic nanotubes do not exhibit PL, so the technique is limited to semiconducting nanotubes, and surface interactions can greatly quench PL for nanotubes on a substrate. In addition, PL imaging requires the detection of near-infrared light for most nanotubes, which necessitates the use of a specialized array detector made from a material such as InGaAs. Although the detection efficiency of existing InGaAs detectors is comparable to that of CCDs, their low pixel resolution and much higher noise level often results in a poor signal-to-noise ratio.

### Optical imaging of graphene

The recent exponential growth of the field of graphene research was catalyzed by the optical imaging technique first used by Geim and Novoselov [5]. If silicon with an appropriate oxide thickness is used as a substrate, even single-layer graphene will be visible under white light illumination because of the optical-interference-induced color change. This technique enabled the rapid identification of single-layer exfoliated graphene for use in a wide range of studies. Similarly, because the optical absorption per graphene layer is measured to be around 2.3% for most of the visible range, single-layer graphene on a transparent substrate can be distinguished in a transmission geometry, and the number of layers can be counted [19].

Imaging and characterizing graphene on arbitrary substrates can be also performed using micro-Raman imaging. The Raman spectrum of graphene shows three prominent peaks, D, G and G' (or 2D), that are also found in CNT Raman spectra. These peaks, like those in the Raman spectra of CNTs, carry useful information about the material's doping level and defect density. In addition, the intensity ratio between the G' peak and the G peak is much larger for single-layer graphene than for bilayer or multilayer graphene [8] (Figure 6(a)). Strained single-layer graphene shows two distinct G peaks that can be used to identify the graphene crystal orientation, based on their separation and polarization dependence [54].

Confocal Raman maps of graphene are typically generated by plotting a metric of the Raman spectrum that correlates with a spatially varying property of the graphene film, such as graphene location (G-band intensity), defect density (D-band intensity or D/G ratio), proportion of single-layer graphene (G'/G ratio), or local doping or strain (G and G' peak position). These mappings are particularly useful for characterizing graphene films grown by CVD techniques, thereby providing spatially resolved information about growth quality. They can be also used to measure growth rate by alternating  $^{12}\text{C}$  and  $^{13}\text{C}$  sources [17] (Figure 6(b)). This can be performed at various stages of processing and fabrication regardless of the sample substrate, be it a growth substrate (such as copper or nickel), a transfer substrate (transparent quartz or silicon) or none at all (suspended graphene). As with CNTs, performing Raman imaging in a wide-field geometry allows graphene to be imaged over a large area in a matter of seconds [50], thus significantly shortening the time required to characterize a CVD-grown sample.

### Photoelectric imaging of carbon nanotubes

Optical excitation of CNTs and graphene can generate electrical signals as well as optical signals. Because these materials are good conductors of electric current, attaching the CNT or graphene sample to metal contacts allows the detection of electrical signals. Additional 'photoelectric imaging' modes are achieved by mapping electrical signals as a function of the position of confocal laser excitation.

Photoelectric signals in CNTs originate from optically excited excitons (Figure 1(b)). These excitons follow one of three main decay pathways: they can recombine radiatively and emit photons, recombine non-radiatively and produce heat, or dissociate into separated electron-hole ( $e-h$ ) pairs. Although the first pathway can be detected using the purely optical methods discussed previously, photoelectric imaging is sensitive to the latter two decay pathways by monitoring changes in the CNT's electrical properties as a result of laser excitation.

The general experimental scheme for photoelectric imaging in CNT- or graphene-based devices involves a confocal microscope with laser- or sample-scanning capability (Figure 7(a)). An image is formed by measuring the current or voltage in the device as a function of laser position while the laser scans across the surface. Reflected and transmitted light can be monitored simultaneously in order to provide an optical image for comparison. The location, intensity and polarity of the photoelectric signal from these images can also be used to probe a combination of the intrinsic electrical and/or thermal properties of CNTs.

This scheme has recently been used to image and electrically characterize individual CNTs in large-scale nanotube networks using a technique known as photothermal current imaging [55]. In this photoelectric imaging mode, a small bias is applied across the nanotube device and the change in conductance is monitored with respect to laser position. Figure 7(b) shows a clearly resolved photothermal current image of a CNT bridging two electrodes. The photothermal current signal is due to the laser-induced thermal excitation of the CNT. When the nanotube absorbs the laser light, the non-radiative decay of excitons generates an excess phonon population, which produces heat. This causes the nanotube's temperature to rise locally, thus reducing (enhancing) the electrical conductance of metallic (semiconducting)

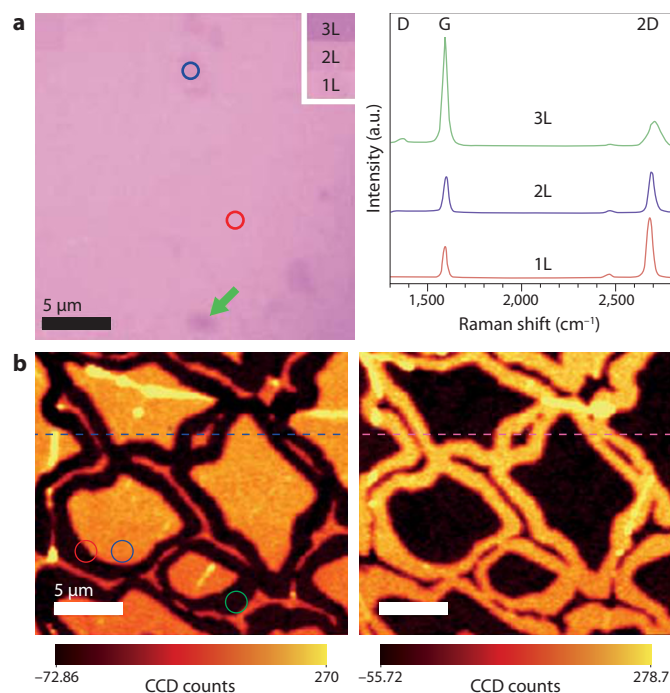


**Figure 6.** (a) A white-light reflection image of graphene on Si/SiO<sub>2</sub> (285 nm). Slight contrast changes indicate areas where multiple layers of graphene are present. Raman spectra taken at these points (right) confirm that the number of graphene layers changes due to a decrease in the 2D/G ratio and a broadening of the 2D peak. Adapted from Ref. 10 (© 2009 AAAS). (b) Confocal Raman maps of the G-band intensity of <sup>13</sup>C (left) and <sup>12</sup>C (right) in CVD graphene grown on copper, where <sup>13</sup>C and <sup>12</sup>C sources were alternated during graphene growth. The G-band peaks position of <sup>12</sup>C and <sup>13</sup>C are different because the heavier nucleus red-shifts the G-band phonon mode slightly, allowing the two sources to be differentiated. These images can be used to map growth vs time and to study the growth mechanism of CVD graphene on various substrates. Adapted from Ref. 17 (© 2009 ACS).

nanotubes. The photothermal heating effect can also be measured optically, as discussed previously (Figure 4(a)).

The change in conductance produced by the laser is proportional to the original conductance of the nanotube, which allows one to directly measure the relative conductance of individual CNTs under different gate biases and thus to distinguish metallic nanotubes from semiconducting nanotubes. As an example, Figure 7(d) shows the gate dependence of the photothermal current signal (blue) with the laser fixed on the body of the CNT shown in Figure 7(b), together with the measured the direct-current conductance (black). A close correlation is clearly observed for all gate biases. Unlike traditional electrical measurements, photothermal current imaging can be used to probe the electrical properties of individual nanotubes even when many CNTs are connected in parallel, as the local optical excitation ensures that only one conduction pathway is perturbed at a time. This could greatly simplify device fabrication and allow for rapid characterization of CNTs on a large scale. Figure 7(e) shows a composite, three-dimensional optical and photothermal current image of a device comprising a group of nanotubes connected between two electrodes. The photothermal signal of each CNT can be clearly resolved despite their close proximity, allowing each CNT to be individually characterized even though they are all electrically parallel.

This measurement scheme can also be used to perform a photoelectric characterization technique known as photocurrent microscopy, in which the zero-bias electrical current in the device is monitored as a function of laser position [56–59]. Instead of monitoring the change in conductance, this technique directly measures the laser-induced current or voltage, which is mainly caused by excitons separating into  $e-h$  pairs and then collecting at the contacts as electric

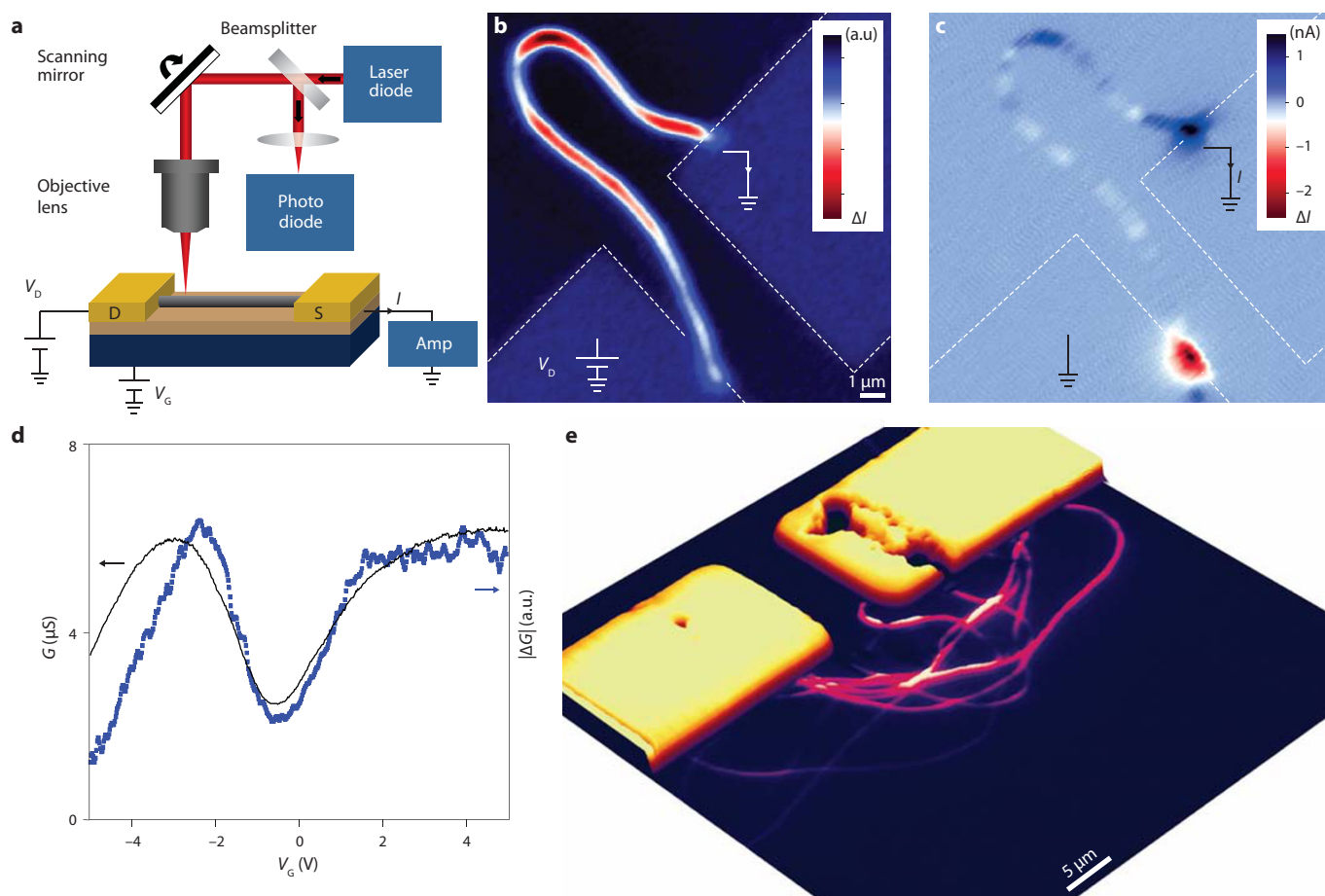


**Figure 7.** (a) Schematic illustration of a photoelectric imaging set-up. A nanotube is electrically contacted such that the electrical response to a localized optical excitation can be probed. An image is constructed by mapping the electrical response as a function of scanning laser position. (b) Photothermal current and (c) photocurrent images of a single CNT device, with electrodes indicated by dashed lines. The photothermal current image maps out the entire length of the nanotube, while the photocurrent signal is strong mainly at the electrical contacts. (d) Gate dependence of photothermal current signal with the laser fixed on the CNT under direct-current conductance. Photothermal current is proportional to overall device conductance. (e) Composite three-dimensional optical and photothermal current image of a multi-nanotube device. Individual CNTs are resolved despite close bundling. Adapted from Ref. 55 (© 2009 NPG).

current. Laser-induced heating can also generate a thermoelectric potential, which partly contributes to photocurrent signals in CNTs and graphene. Although this is not strictly an imaging technique, the intensity and polarity of the photocurrent carry useful information regarding the local electrostatic potential or electric field along the nanotube. The strongest (and sometimes only) signal is seen near the electrode contacts or at interfaces between two different dielectric environments [59,60], as shown in the zero-bias photocurrent image in Figure 7(c). Photoelectric microscopy has also been used to study various graphene-based devices [61–64]; strong photoelectric signals have been observed near metal electrodes in both two-electrode [61] and multi-electrode devices [61,62], at internal p–n junctions [63] and near interfaces between single-layer and bilayer regions [64].

## Summary and perspectives

Optically imaging and characterizing individual nanostructures at high spatial and temporal resolutions remains an important and long-standing challenge. Below we discuss areas of development for these optical techniques.

### Deep-UV resonance imaging of graphene and carbon nanotubes

Most of the techniques discussed in the previous sections use a visible or near-infrared laser source, but imaging CNTs and graphene at deep-UV wavelengths (below 300 nm) may provide several advantages. First, all CNTs, regardless of their diameter or chiral index, have a universal

resonance in this wavelength range. This is due to a saddle point resonance in the graphene electronic band structure at around 4.6 eV [65]. Second, deep-UV imaging could provide enhanced spatial resolution (as good as 100 nm) due to its shorter wavelength. Third, scattered intensity (Rayleigh and Raman) increases as  $\lambda^{-1}$  for CNTs [29], so scattered signals in the deep-UV should be stronger than those based on visible or near-infrared light. However, deep-UV illumination and detection requires specially designed optical components (fused silica or mirror-based optics) and light sources (deep-UV lasers or xenon light sources).

### Signal enhancement through stimulated emission

Stimulated emission microscopy offers another way to enhance the signal produced by Raman and PL processes. In this imaging mode, two pulsed lasers of different wavelengths are simultaneously delivered onto the same focused spot. If the energy difference between the two lasers matches a known Raman transition, stimulated emission can occur, causing the absorption of one beam to be strongly correlated with the intensity of the other. This modulation of laser absorption can be monitored for high-speed and high-efficiency Raman imaging. Stimulated emission microscopy has recently been shown to enhance the signal-to-noise ratio of inefficient or forbidden optical processes by several orders of magnitude, enabling video-rate Raman and fluorescence imaging of biological samples in liquid [66,67]. This capability could also be used to greatly improve carbon nanostructure imaging, especially in solvent-dispersed systems.

### Combining near-field and nonlinear optical techniques

A number of near-field optical techniques provide ways of improving the spatial resolution of optical imaging beyond the diffraction limit. One such technique has been used to image CNTs at resolutions smaller than 15 nm using both Raman and PL detection [68], thus providing high-spatial-resolution information about individual defects in a nanotube. Several nonlinear optical imaging techniques have recently been reported, all of which could soon offer the ability to image CNTs at short time resolutions. Four-wave-mixing techniques for detecting coherent anti-Stokes Raman scattering [69] and pump-probe techniques for measuring transient absorption [70] have both been used to successfully image individual SWNTs. Combining nonlinear and near-field optical techniques could create a powerful imaging platform for CNTs and graphene with nanoscale spatial resolution and femtosecond time resolution, providing new insights into exciting areas such as the spatiotemporal dynamics of excitons, the role of CNT-substrate interactions, the electrical and optical properties near individual defects and internal p-n junctions, and the properties of edges and grain boundaries in graphene.

The laser-based imaging techniques reviewed here have played an essential role in the identification and characterization of carbon nanostructures. They also have potential uses as a powerful means not only to identify lattice defects in such structures, but also to study their physical and chemical properties, as well as probe the charge and energy transfer between adjacent nanostructures on substrates and in solutions. Perhaps one of the most exciting applications of laser-based imaging is to directly 'watch' and ultimately control the growth of carbon nanostructures in real time. Thanks to the high imaging speeds provided by a wide-field illumination geometry [16,50] and the future development of powerful stimulated imaging techniques, laser-based imaging could provide advantages over previous microscopy techniques (such as environmental TEM [71] or low-energy electron microscopy [11]) for the *in situ* characterization of growth. In particular, optical techniques are compatible with most reaction conditions, require relatively simple instrumentation and can acquire images and spectroscopic information simultaneously. These techniques are therefore ideal for providing new insights about the growth rate, spatial distribution and defect density of CNTs and graphene over large areas in real time, while customizing the physical and chemical properties of the resulting materials.

### Acknowledgments

This work was supported by the Air Force Office of Scientific Research and an Alfred P. Sloan Research Fellowship. Additional funding was received from the National Science Foundation through an NSF CAREER grant. R. W. H. is supported by a Graduate Research Fellowship from the National Science Foundation. H. C. C. acknowledges the support of the National Research Foundation of Korea EPB center (2010-001779) and World Class University (WCU) program (R31-2008-000-10059-0).

### References

1. A. Jorio, G. Dresselhaus, M. S. Dresselhaus, *Carbon Nanotubes. Advanced Topics in the Synthesis, Structure, Properties and Applications* (Springer-Verlag, 2008).
2. A. K. Geim, *Science* **324**, 1530 (2009).
3. S. Iijima, *Nature* **354**, 56 (1991).
4. S. Iijima, T. Ichihashi, *Nature* **363**, 603 (1993).
5. K. S. Novoselov *et al.*, *Proc. Nat. Acad. Sci.* **102**, 10451 (2005).
6. M. Gao *et al.*, *Appl. Phys. Lett.* **82**, 2703 (2003).
7. T. W. Odom, J.-L. Huang, P. Kim, C. M. Lieber, *Nature* **391**, 62 (1998).
8. A. Reina *et al.*, *Nano Lett.* **9**, 30 (2009).
9. K. S. Kim *et al.*, *Nature* **457**, 706 (2009).
10. X. S. Li *et al.*, *Science* **324**, 1312 (2009).
11. J. M. Wofford, S. Nie, K. F. McCarty, N. C. Bartelt, O. D. Dubon, *Nano Lett.* **10**, 4890 (2010).
12. X. S. Li *et al.*, *Nano Lett.* **10**, 4328 (2010).
13. P. Y. Huang *et al.*, *Nature* **469**, 389 (2011).
14. K. Kim *et al.*, *ACS Nano* **5**, 2142 (2011).
15. D. Y. Joh *et al.*, *Nano Lett.* **11**, 1 (2011).
16. K. Kaminska, J. Lefebvre, D. G. Austing, P. Finnie, *Nanotechnol.* **18**, 165707 (2007).
17. X. S. Li, W. W. Cai, L. Colombo, R. S. Ruoff, *Nano Lett.* **9**, 4268 (2009).
18. T. Ando, *NPG Asia Mater.* **1**, 17 (2009).
19. R. R. Nair *et al.*, *Science* **320**, 1308 (2008).
20. F. Wang, G. Dukovic, L. E. Brus, T. F. Heinz, *Science* **308**, 838 (2005).
21. F. Wang *et al.*, *Phys. Rev. Lett.* **99**, 227401 (2007).
22. M. Y. Sfeir *et al.*, *Science* **312**, 554 (2006).
23. T. Hertel *et al.*, *Nano Lett.* **5**, 511 (2005).
24. M. Y. Sfeir *et al.*, *Science* **306**, 1540 (2004).
25. S. M. Bachilo *et al.*, *Science* **298**, 2361 (2002).
26. A. Hartschuh, H. N. Pedrosa, L. Novotny, T. D. Krauss, *Science* **301**, 1354 (2003).
27. F. Schöppler *et al.*, *J. Phys. Chem. C* **115**, 14682 (2011).
28. S. Berciaud, L. Cognet, B. Lounis, *Phys. Rev. Lett.* **101**, 077402 (2008).
29. D. Y. Joh *et al.*, *Nature Nanotechnol.* **6**, 51 (2011).
30. J. E. Bohn *et al.*, *ACS Nano* **4**, 3466 (2010).
31. J. Lefebvre, D. G. Austing, J. Bond, P. Finnie, *Nano Lett.* **6**, 1603 (2006).
32. S.-Y. Ju, W. P. Kopcha, F. Papadimitrakopoulos, *Science* **323**, 1319 (2009).
33. J. Crochet, M. Clemens, T. Hertel, *J. Am. Chem. Soc.* **129**, 8058 (2007).
34. K. Kaminska, J. Lefebvre, D. G. Austing, P. Finnie, *Phys. Rev. B* **73**, 235410 (2006).
35. Y. Zhang *et al.*, *J. Phys. Chem. C* **111**, 1983 (2007).
36. M. Steiner *et al.*, *Appl. Phys. A* **96**, 271 (2009).
37. J. Lefebvre, J. M. Fraser, P. Finnie, Y. Homma, *Phys. Rev. B* **69**, 075403 (2004).
38. G. S. Duesberg, I. Loa, M. Burghard, K. Syassen, S. Roth, *Phys. Rev. Lett.* **85**, 5436 (2000).
39. M. S. Dresselhaus, G. Dresselhaus, R. Saito, A. Jorio, *Phys. Rep. Rev. Sect. Phys. Lett.* **409**, 47 (2010).
40. S. Berciaud *et al.*, *Phys. Rev. B* **81**, 041414(R) (2010).
41. H. Kataura *et al.*, *Synthetic Met.* **103**, 2555 (1999).
42. S. Berciaud, L. Cognet, G. A. Blab, B. Lounis, *Phys. Rev. Lett.* **93**, 257402 (2004).
43. S. Berciaud, L. Cognet, P. Poulin, R. B. Weisman, B. Lounis, *Nano Lett.* **7**, 1203 (2007).
44. S. D. M. Brown *et al.*, *Phys. Rev. B* **63**, 155414 (2001).
45. A. Jorio *et al.*, *Phys. Rev. B* **65**, 155412 (2002).
46. P. Corio, A. Jorio, N. Demir, M. S. Dresselhaus, *Chem. Phys. Lett.* **392**, 396 (2004).
47. S. K. Doorn *et al.*, *J. Phys. Chem. B* **109**, 3751 (2005).
48. C. Fantini *et al.*, *Phys. Rev. Lett.* **93**, 147406 (2004).
49. L. Zhang, Z. Jia, L. M. Huang, S. O'Brien, Z. H. Yu, *J. Phys. Chem. C* **111**, 11240 (2007).
50. R. Havener, S. Y. Ju, M. Segal, L. Herman, J. Park, *APS March Meeting* (2011), <http://meetings.aps.org/link/BAPS.2011.MAR.P28.8>
51. M. J. O'Connell *et al.*, *Science* **297**, 593 (2002).
52. K. Welsher, Z. Liu, D. Daranciang, H. Dai, *Nano Lett.* **8**, 586 (2008).
53. D. A. Tsybouski, S. M. Bachilo, R. B. Weisman, *Nano Lett.* **5**, 975 (2005).
54. M. Y. Huang *et al.*, *Proc. Nat. Acad. Sci.* **106**, 7304 (2009).
55. A. W. Tsen, L. A. K. Donev, H. Kurt, L. H. Herman, J. Park, *Nature Nanotechnol.* **4**, 108 (2009).
56. K. Balasubramanian, M. Burghard, K. Kern, M. Scolari, A. Mews, *Nano Lett.* **5**, 507 (2005).
57. E. J. H. Lee *et al.*, *Small* **3**, 2038 (2007).
58. M. Freitag *et al.*, *Nano Lett.* **7**, 2037 (2007).
59. Y. H. Ahn, A. W. Tsen, B. Kim, Y. W. Park, J. Park, *Nano Lett.* **7**, 3320 (2007).
60. N. M. Gabor, Z. H. Zhong, K. Bosnick, J. Park, P. L. McEuen, *Science* **325**, 1367 (2009).
61. E. J. H. Lee, K. Balasubramanian, R. T. Weitz, M. Burghard, K. Kern, *Nature Nanotechnol.* **3**, 486 (2008).
62. J. Park, Y. H. Ahn, C. Ruiz-Vargas, *Nano Lett.* **9**, 1742 (2009).
63. T. Mueller, F. Xia, M. Freitag, J. Tsang, P. Avouris, *Phys. Rev. B* **79**, 245430 (2009).
64. X. D. Xu, N. M. Gabor, J. S. Alden, A. M. van der Zande, P. L. McEuen, *Nano Lett.* **10**, 562 (2010).
65. K. F. Mak, J. Shan, T. F. Heinz, *Phys. Rev. Lett.* **106**, 046401 (2011).
66. C. W. Freidiger *et al.*, *Science* **322**, 1857 (2008).
67. W. Min *et al.*, *Nature* **461**, 1105 (2009).
68. A. Hartschuh, H. H. Qian, A. J. Meixner, N. Anderson, L. Novotny, *Nano Lett.* **5**, 2310 (2005).
69. H. Kim, T. Sheps, P. G. Collins, E. O. Potma, *Nano Lett.* **9**, 2991 (2009).
70. Y. Jung *et al.*, *Phys. Rev. Lett.* **105**, 217401 (2010).
71. M. Lin *et al.*, *Nano Lett.* **7**, 2234 (2007).

## Author profiles



### Robin W. Havener

Robin W. Havener received her BSE degree in materials science and engineering from the University of Pennsylvania, USA, in 2008. She is currently a doctoral student in applied physics at Cornell University. Her current research interests include wide-field optical imaging and spectroscopy of carbon nanotubes and graphene.



### Hee Cheul Choi

Hee Cheul Choi earned his PhD degree in chemistry from Purdue University, USA, in 2001. After postdoctoral research at Stanford University, USA, he joined the faculty of the Department of Chemistry at Pohang University of Science and Technology (POSTECH), Korea, in 2003, and is currently Hongdeok Young Chaired Professor. His research interests include self-crystallization of highly conjugated molecules for the development of new electrical and optical systems, correlation studies between structural geometry and electrical/optical properties, and photothermal/photodynamic biotherapeutics using optically active nanomaterials.



### Adam W. Tsen

Adam W. Tsen is a PhD candidate in applied physics at Cornell University, USA. He received his BS degree in physics and electrical engineering at the University of California, Berkeley in 2006. His current research interest is in the spatially resolved characterization of electrical transport in carbon nanostructures.



### Jiwoong Park

Jiwoong Park is an assistant professor in the Department of Chemistry and Chemical Biology at Cornell University, USA, with a PhD in physics from the University of California, Berkeley, USA. Before coming to Cornell University, he was a junior fellow of the Rowland Institute at Harvard University, USA. His research interests focus on the electronic and optical properties of nanoscale materials including semiconductor nanowires, carbon nanotubes and graphene.